# Nanoscale Advances

This article can be cited before page numbers have been issued, to do this please use: Z. Tang, J. Zhao, H. Liu, B. Huang, F. hang, N. Cheng, Z. Liu and P. Zong, *Nanoscale Adv.*, 2026, DOI: 10.1039/D6NA00481D.

View Article Online
DOI: 10.1039/D6NA00481D

# Simple CsI Doping Outperforms Complex Organic Additives in Carbon–Based Perovskite Solar Cells

Zhe Tang[1, 2], Jiawei Zhao[2, 3], Heng Liu[1, 4, *], Baoting Huang[2], Fengling Hang[2], Nian Cheng[5], Zhen–guo Liu[1, 2, 3 *], Peng–an Zong[1, 2, *]

[1] College of Materials Science and Engineering, Nanjing Tech University, Nanjing 211800, China

[2] Key Laboratory of Flexible Electronics of Zhejiang Province, Ningbo Institute of Northwestern Polytechnical University, Ningbo 315103, China

[3] Frontiers Science Center for Flexible Electronics (FSCFE), Institute of Flexible Electronics (IFE), Northwestern Polytechnical University, Xian 710072, China

[4] Advanced Institute for Materials Research (WPI-AIMR), Tohoku University, Senda, Japan

[5] School of Physics and Optoelectronic Engineering, Yangtze University, Jingzhou 434023, China

* Corresponding Author: pazong@njtech.edu.cn (Dr. Peng–an Zong), iamzgliu@nwpu.edu.cn (Dr. Zhen–guo Liu), heng.liu.e1@tohoku.ac.jp (Dr. Heng Liu)

View Article Online
DOI: 10.1039/D6NA00481D

## Abstract:

Carbon–based hole–transport–layer (HTL)–free perovskite solar cells (C–PSCs) have emerged as promising candidates for commercialization, owing to their low cost, high stability, and simple device architecture. Nevertheless, the performance of C–PSCs is still limited by inconsistent perovskite film quality and high defect density. While cesium iodide (CsI) doping has been explored in perovskite systems, its application in HTL–free C–PSCs remains relatively underinvestigated and often yields only limited performance improvements, particularly in single–cation systems or with the aid of additional interlayers or additives. In this work, we report a facile yet effective strategy of incorporating CsI into MA/FA dual–cation perovskite films via a one–step spin–coating process–without any other interlayer or organic passivation additives. The incorporation of $Cs^+$ significantly enhances crystallization quality and induces lattice contraction which synergistically suppresses the formation of intrinsic defects and non–perovskite phasesmitigates ion migration, and improves phase stability. As a result, the champion CsI–doped C–PSC achieves a remarkable power conversion efficiency (PCE) of 17.31%, substantially outperforming the control device (13.25%) fabricated under identical conditions. Furthermore, the CsI–incorporated devices demonstrate exceptional long–term operational stability, retaining 73% of their initial PCE after 30 days of storage in ambient air. This work highlights the potential of inorganic cation engineering in realizing high–performance, low–cost, and durable C–PSCs through a simple and scalable process.

Keywords: Carbon–based Perovskite Solar Cells, HTL–free, Additive engineering, Energy level alignment, Reduction in grain boundaries

View Article Online
DOI: 10.1039/D6NA00481D

## 1. Introduction

Organic–inorganic hybrid perovskite solar cells (PSCs) have witnessed unprecedented progress in photovoltaic performance, with the certified power conversion efficiency (PCE) soaring from the 3.9% to over 27% within a decade [1–5]. Such remarkable advancement is largely attributable to their excellent optoelectronic properties and facile solution processability [6–9]. Nevertheless, the majority of high–efficiency PSCs still rely on expensive organic hole–transport–layer (HTL) coupled and noble–metal electrodes (e.g., gold), which not only increase material costs but also introduce concerns over operational instability, thereby hindering large–scale commercialization [10,11]. In this context, carbon–based hole–transport–layer (HTL)–free perovskite solar cells (C–PSCs) have emerged as a promising alternative. By utilizing carbon materials as both the electrode and the hole–extraction layer, C–PSCs eliminate the need for specialized HTMs and vacuum–processed metal electrodes, significantly reducing fabrication cost and simplifying device architecture [12]. In addition, carbon electrodes exhibit intrinsic advantages such as high hydrophobicity, good electrical conductivity, remarkable environmental stability, and strong resistance to ion migration, collectively enhancing device durability under ambient conditions [13,14].

Despite these merits, the performance of C–PSCs still lags behind that of conventional n–i–p or p–i–n structured devices. One key challenge lies in the quality of the perovskite absorber layer. Although methylammonium lead iodide ($MAPbI_3$) has been widely adopted in C–PSCs its low–temperature processability, its relatively narrow bandgap and moderate stability restrict further efficiency improvements [15]. Formamidinium lead iodide ($FAPbI_3$), with a broader absorption range and enhanced thermal stability, presents a more ideal candidate for high–performance photovoltaics [16]. However, a significant challenge lies in its phase instability, as the photocurrent–generating black perovskite phase (α–phase) readily converts into a non–photoactive yellow δ–phase (hexagonal phase) at ambient conditions [17]. Mixing $FA^+$ with $MA^+$

View Article Online
DOI: 10.1039/D6NA00481D

helps stabilize the black perovskite phase, yet the mismatch in crystallization kinetics between $FAPbI_3$ and $MAPbI_3$ often results in films with high defect density and compromised reproducibility [16].

To address these issues, inorganic cation doping–particularly with cesium ($Cs^+$) has been widely employed. It has been shown that $Cs^+$ incorporation can optimize the Goldschmidt tolerance factor, improve phase stability, and passivate intrinsic defects [18–20]. For example, Zhen et al. demonstrated that a small amount of $Cs^+$ promotes the formation of the desired black perovskite phase in $FAPbI_3$ by modulating crystallization kinetics [18]. Despite these successes, most reported Cs–doped high–efficiency PSCs still rely on complex multi–layer structures or additional organic passivators. More importantly, the potential of CsI doping in simplifying the device stack–specifically in HTL–free, carbon–electrode–based architectures–has been underexplored. For instance, Wang et al. incorporated CsI into a $MAPbI_3$–based C–PSC and achieved a PCE of 10.57% [21], indicating limited gain in single–cation systems. In other cases, $Cs^+$ doping was coupled with extra interlayers or additional additives to boost performance. For example, Xu et al. introduced a CuSCN layer following Cs doping in the perovskite layer for passivation [22], which complicates fabrication and undermines the cost advantage of C–PSCs. Wang et al. reported a PCE of 14.15% in $Cs^+$–doped C–PSCs, which required the intricate APH additive for passivation, thereby complicating manufacture and raising costs [23]. It is important to note that the highest reported efficiency for C–PSCs (>22%) was realized on a printable mesoscopic $TiO_2$/$ZrO_2$/carbon triple–layer scaffold, where the insulating $ZrO_2$ spacer and multiple infiltration steps enable superior charge collection and mechanical robustness [3]. In contrast, a much simpler planar architecture–consisting only of ITO/SnO2/perovskite/carbon without any hole–transporting layer or additional interlayer–offers significant advantages in fabrication simplicity and cost, yet typically yields lower efficiencies in the 13–15% range due to the absence of dedicated charge–selective contacts and interfacial engineering. These two device

View Article Online
DOI: 10.1039/D6NA00481D

configurations are fundamentally different and cannot be directly compared in terms of absolute efficiency, as the mesoscopic scaffold inherently provides more favorable charge extraction pathways and structural stability. Therefore, achieving high efficiency in the planar HTL–free C–PSC through minimalistic approaches remains a distinct and worthwhile challenge.

Herein, we demonstrate that strategic incorporation of CsI into MA/FA mixed–cation perovskite films using a straightforward one–step spin–coating process, without any additional interlayers or organic passivation agents, can synergistically enhance film quality, optoelectronic properties, and device performance. The small ionic radius of $Cs^+$ promotes lattice contraction, facilitating the growth of highly crystalline, phase–pure perovskite films while suppressing the formation of non–perovskite phases and iodide vacancies. This multifunctional doping strategy not only improves crystallization but also significantly reduces defect–mediated non–radiative recombination and ion migration. As a result, we achieved a champion PCE of 17.31% with excellent operational stability–far surpassing the control device (PCE = 13.25%), while retaining 73% of the initial PCE after 30 days of storage under ambient conditions. This work highlights the viability of all–inorganic cation engineering as a simple yet effective route toward high–performance, low–cost, and durable carbon–based perovskite photovoltaics.

## 2. Results and Discussion

$Cs_x(MA_{0.9}FA_{0.1})_{1-x}PbI_3$ thin films were fabricated via a one–step spin coating process. **Fig. 1a** displays the X–ray diffraction (XRD) patterns of perovskite films prepared with varying concentrations of CsI dopant. It is observed that the diffraction peaks corresponding to the (110) and (220) crystallographic planes of the black α–phase perovskite intensify progressively with increasing $Cs^+$ content indicating that an optimal amount of CsI promotes preferential crystal orientation and enhances the phase purity of the perovskite. As shown in the magnified view of the (110) diffraction peak (**Fig. S1)**, a slight shift toward

View Article Online
DOI: 10.1039/D6NA00481D

higher angles is observed upon 5 mol% CsI incorporation (denoted as Cs–0.05). This shift can be attributable to lattice contraction resulting from the incorporation of $Cs^+$, which has a smaller ionic radius–into the perovskite lattice, partially substituting the larger $MA^+$ and $FA^+$ cations [40, 41].

Concurrently, all XRD patterns exhibit a characteristic peak at 12.7°, corresponding to the (001) plane of $PbI_2$. This signal likely originates from incomplete perovskite conversion and moisture–induced decomposition during annealing in ambient air. Following CsI doping, the intensity of the $PbI_2$ (001) peak gradually decreases, reaching a minimum at the optimal doping level of 5 mol% Cs, where perovskite crystallinity is maximized. In contrast, excessive $Cs^+$ doping leads to an increase in $PbI_2$ signal and attenuation of the perovskite diffraction peaks, consistent with previously reported detrimental lattice distortion at high doping levels [24]. These results demonstrate that moderate $Cs^+$ incorporation facilitates a more stable perovskite structure [25], whereas supra–optimal doping disrupts the structural equilibrium and degrades the film quality.

To elucidate the role of $Cs^+$ doping in microstructure evolution, scanning electron microscopy (SEM) was performed on perovskite films with varying Cs concentrations (**Fig. 1b–e**). The control film exhibits fine grains with abundant grain boundaries that hinder carrier transport via scattering, thereby degrading mobility. Widespread crystalline debris and pinholes further introduce trapping states that accelerate non–radiative recombination and limit carrier lifetimes [26]. Incorporation of 5 mol% CsI, however, triggers pronounced grain coarsening and a concurrent decline in boundary density and pinhole formation, substantially improving morphological homogeneity. This originates from $Cs^+$–mediated nucleation modulation, whereby retarded nucleation kinetics depress nucleus density and favor grain growth through preferential Ostwald ripening [27, 28]. Grain size statistics (**Fig. 1f, g)** confirm an increase from 193.91 nm

View Article Online
DOI: 10.1039/D6NA00481D

(undoped) to 268.81 nm (Cs–doped). This microstructural coarsening not only enhances photon capture but also curtails defect–assisted recombination, leading to superior charge transport characteristics [29, 30].

Energy–dispersive X–ray spectroscopy (EDS) mapping of $Cs_x(MA_{0.9}FA_{0.1})_{1-x}PbI_3$ film confirms homogeneous Cs dispersion in the film with no localized aggregation (**Fig. S2**), confirming effective lattice incorporation. Atomic force microscopy (AFM, **Fig. 1h, i**) further reveals significant surface smoothing upon CsI modification: the RMS roughness decreases from 18.6 nm in the control to 9.55 nm in the doped film, indicating improved surface uniformity. The resulting planarization fosters better perovskite/carbon electrode contact, which suppresses interfacial recombination and raises charge extraction efficiency.

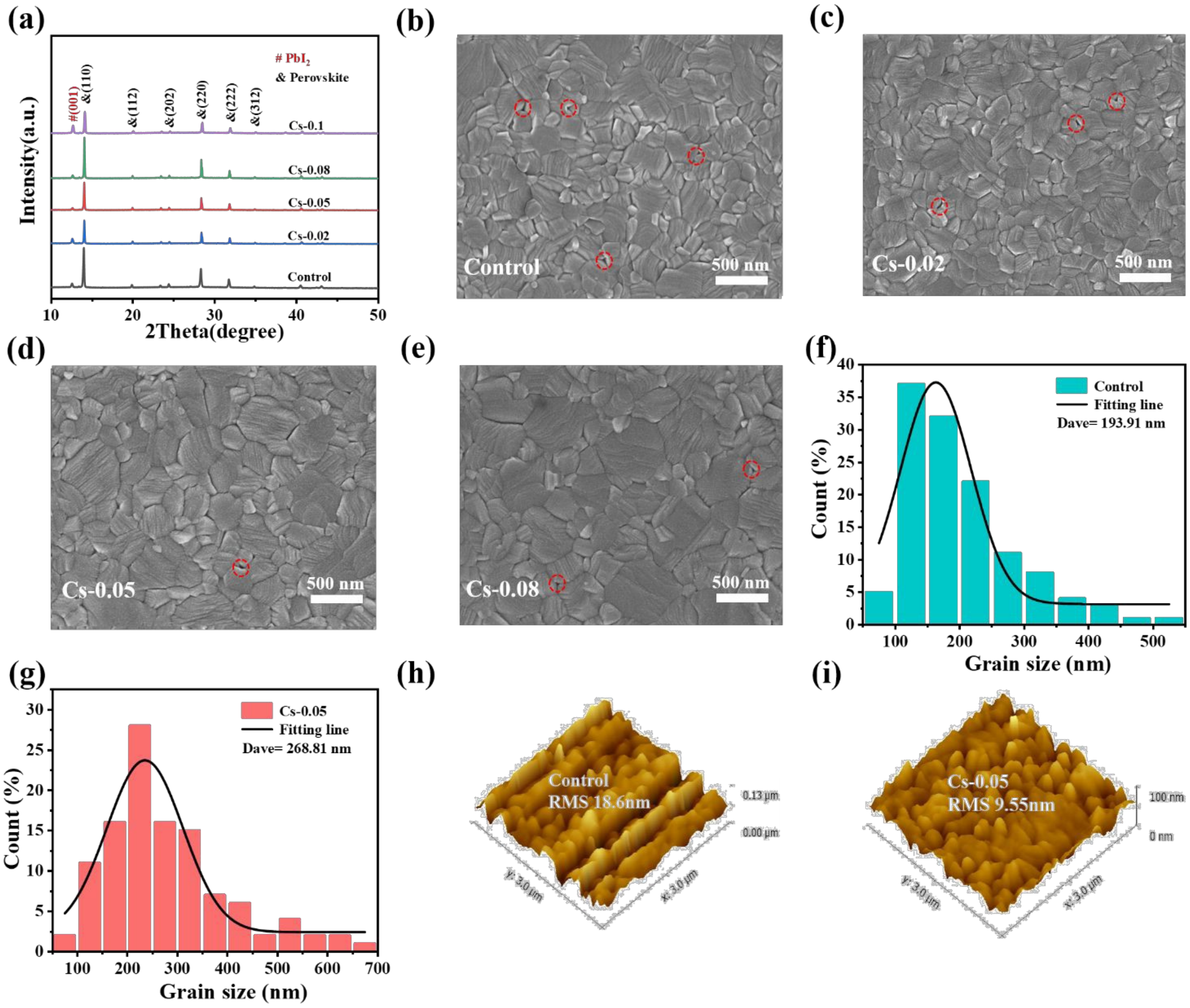

View Article Online
DOI: 10.1039/D6NA00481D

**Figure 1 a** XRD of perovskite films with different concentrations of CsI. **b–e** SEM images of perovskite films with different concentrations of CsI additives: (d) Control, (e) Cs–0.02, (f) Cs–0.05, (g) Cs–0.08. **f–g** Average grain size of perovskite films with different concentrations of CsI additives: (h) Control, (i) Cs–0.05. **h** AFM image of the control group perovskite film. **i** AFM image of perovskite film doped with CsI.

**Fig. 2a** compares the ultraviolet–visible (UV–Vis) absorption spectra of control and CsI–doped perovskite films, revealing a universal enhancement in absorbance upon doping, especially within the 400–550 nm range. The optimal light–harvesting performance of the Cs–0.05 film arises from the combined benefits of improved morphology and composition. Specifically, larger grain sizes allow photons to travel longer distances within the film, providing more opportunities for absorption, while the suppression of defects minimizes non–productive absorption and scattering [31], in agreement with prior structural characterization. A subtle blueshift of the absorption edge further indicates a doping–induced modification of the band structure. Tauc plot analysis based on Equation (1):

$$(\alpha \mathrm{h}\nu)^{\frac{1}{n}}=B(\mathrm{h}\nu-E_g) \qquad (1),$$

where $\alpha$, $h$, $v$, and $E_g$ represent the absorption coefficient, Planck's constant, frequency and bandgap, respectively, confirms a slight bandgap expansion from 1.586 eV to 1.592 eV with 5 mol% CsI doping (**Fig. 2b** and **c**). To elucidate the electronic origin of this shift, the highest occupied molecular orbital (HOMO) energy levels was determined by photoelectron spectroscopy in air (PESA). Results indicate that the HOMO level shifts upward from –5.68 eV for the control to –5.66 eV for the Cs–0.05 film (**Fig. 2d** and **e**). As summarized in the energy level diagram (**Fig. 2f**), this 0.02 eV valence uplift of band maximum (VBM) reduces the the offset for hole extraction at the perovskite layer/carbon electrode interface, thereby favoring efficient charge extraction and lowering energy losses.

View Article Online
DOI: 10.1039/D6NA00481D

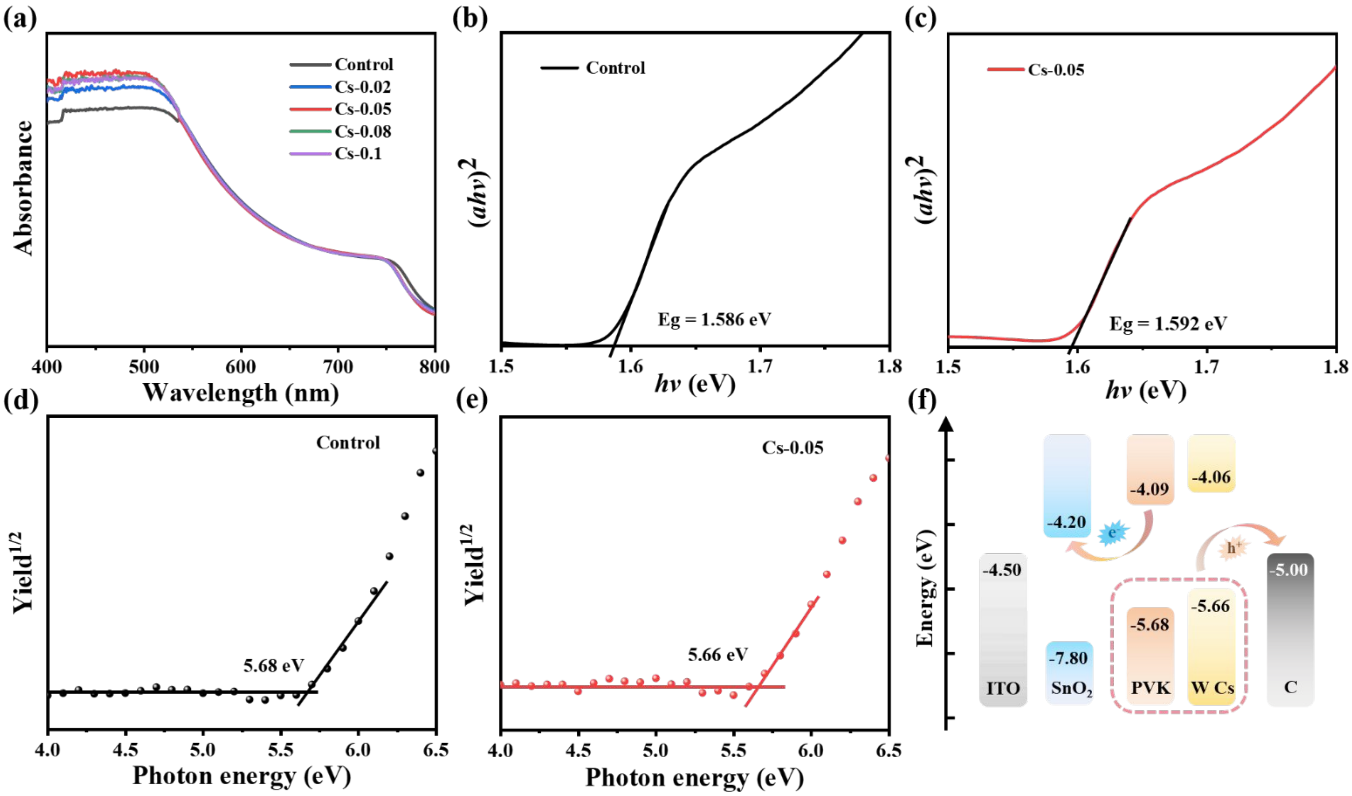

**Figure 2 a** UV–vis absorption spectra. **b–c** Tauc plot: (b) Control; (c) Cs–0.05. **d–e** HOMO energy levels of (d) the control perovskite films and (e) the perovskite films treated with 5 mol% CsI. **f** Energy level diagram of carbon–based PSCs with various perovskite films.

To probe atomic–scale interactions in Cs–doped perovskites, X–ray photoelectron spectroscopy (XPS) was performed on both control and Cs–0.05 samples (**Fig. 3a** and **b**). The Pb 4f and I 3d core–level spectra of the Cs–0.05 film exhibit positive binding energy shifts of 0.15 eV and 0.10 eV, respectively. These shifts are direct fingerprints of the enhanced ionicity and strengthened chemical bonding within the Pb–I framework. The incorporation of smaller $Cs^+$ ions, which partially substitutes the larger $MA^+$/$FA^+$ cations, induces a lattice contraction [32]. This contraction reduces the Pb–I bond length, thereby intensifying the electrostatic interaction. Consequently, the strengthened Pb–I bonding significantly increases the formation energy of iodide vacancies, which are primary defects and channels for ion migration. This mechanistic insight, corroborated by the reduced trap density from SCLC measurements, elucidates how $Cs^+$ doping

View Article Online
DOI: 10.1039/D6NA00481D

fundamentally suppresses defect generation and ion migration, thereby enhancing both the electronic quality and structural stability of the perovskite lattice.

To further evaluate defect–mediated recombination, steady–state photoluminescence (PL) and time–resolved photoluminescence (TRPL) spectra were acquired from films deposited on glass substrates. The Cs–doped film (**Fig. 3c**) exhibits a substantially stronger PL intensity along with a hypsochromic (blue) shift relative to the control, indicating a reduction in non–radiative recombination centers and prolonged carrier lifetimes. The TRPL decay curves were fitted using a biexponential function (Equation 2) :

$$f(t)=A_1 exp(-\frac{t}{\tau_1})+A_2 exp(-\frac{t}{\tau_2}) \qquad (2),$$

where $A_1$ and $A_2$ are the amplitudes, and $\tau_1$ and $\tau_2$ represent the fast and slow decay time constants, associated with radiative and non–radiative recombination processes, respectively [33]. The average carrier lifetime $\tau_{\mathrm{ave}}$ was calculated according to Equation (3):

$$\tau_{ave}=\frac{(A_1\tau_1^2+A_2\tau_2^2)}{(A_1\tau_1+A_2\tau_2)} \qquad (3),$$

Detailed fitting parameters are provided in **Fig. 3d** and **Table S1**. The $\tau_{\mathrm{ave}}$ increases markedly from 253.28 ns to 531.87 ns upon $Cs^+$ incorporation. This improvement is attributed to the lattice contraction and microstructural densification induced by CsI doping, which reduce grain boundary density and void formation, thereby effectively passivating defect states and suppressing non–radiative recombination channels [34].

To quantitatively analyze the trap density ($N_t$), space charge–limited current (SCLC) measurements were performed. As shown in **Fig. 3e** and **f**, the current–voltage ($I$–$V$) characteristics exhibit three distinct regions: an Ohmic region (linear $I$–$V$), a trap–filling region (sharp current rise as traps are filled), and a trap–free Child's region. The trap–filling limit voltage ($V_{\mathrm{TFL}}$) is defined by the intersection of the Ohmic and trap–filling regions. The trap density $N_t$ can be calculated by Equation (4):

View Article Online
DOI: 10.1039/D6NA00481D

$$N_t = \frac{2\varepsilon_0\varepsilon_r V_{TFL}}{eL^2} \quad (4),$$

where $\varepsilon_0$, $\varepsilon_r$, $e$, and $L$ are the vacuum permittivity, the relative permittivity of the perovskite, the elementary charge, and the thickness of the perovskite film, respectively. Based on the values summarized in **Table S2**, the $V_{\mathrm{TFL}}$ values are 0.90 V for the control device and 0.78 V for the Cs–doped device, corresponding to $N_t$ values of $1.56 \times 10^{16}$ cm$^{-3}$ and $1.35 \times 10^{16}$ cm$^{-3}$, respectively. These results confirm that the Cs$^+$ incorporation effectively passivates defects in the perovskite film, thereby suppressing non–radiative recombinations [35].

Electrochemical impedance spectroscopy (EIS) was further employed to investigate the charge transport and recombination behavior. As summarized in **Fig. 3g** and **Table S3**, the series resistance ($R_s$) decreases from 28.18 Ω for the control device to 27.9 Ω after Cs$^+$ doping. This reduction is attributed to the Cs$^+$ induced growth of larger grains and the consequent decrease in grain boundary density, which provide more continuous pathways for charge transport. At the same time, the significantly smoother film surface ensures more intimate contact with the carbon electrode, lowering the interfacial contact resistance. Furthermore, the strengthened Pb–I bonding suppresses ion migration and vacancy-related trapping, thereby improving carrier mobility, while the suppression of non-perovskite phases minimizes insulating impurities that would obstruct charge flow. These combined structural and electronic improvements collectively facilitate more efficient charge extraction. Moreover, recombination resistance ($R_{rec}$) rises significantly from 3087 Ω to 4709 Ω after doping, indicates suppressed interfacial recombination, which is a primary factor responsible for the enhanced $V_{OC}$. Concurrently, the optimized energy alignment, as revealed by the PESA results (Fig. 2f), facilitates charge extraction and and contributes to the improvement in $J_{SC}$ [36]. These synergistic effects collectively boost the overall device performance. As illustrated in **Fig. 3h**, Cs$^+$ ions partially substitute methylammonium sites within the corner–sharing $[\mathrm{PbI_6}]^{4-}$ octahedral framework while maintaining the perovskite structure. Concurrently, Cs$^+$ doping increases the lattice formation energy, which

View Article Online
DOI: 10.1039/D6NA00481D

suppresses the formation of non–perovskite phases, while strengthens Pb–I bonding via increased orbital hybridization. These synergistic effects collectively improve film morphological integrity and operational stability of the perovskite film [28].

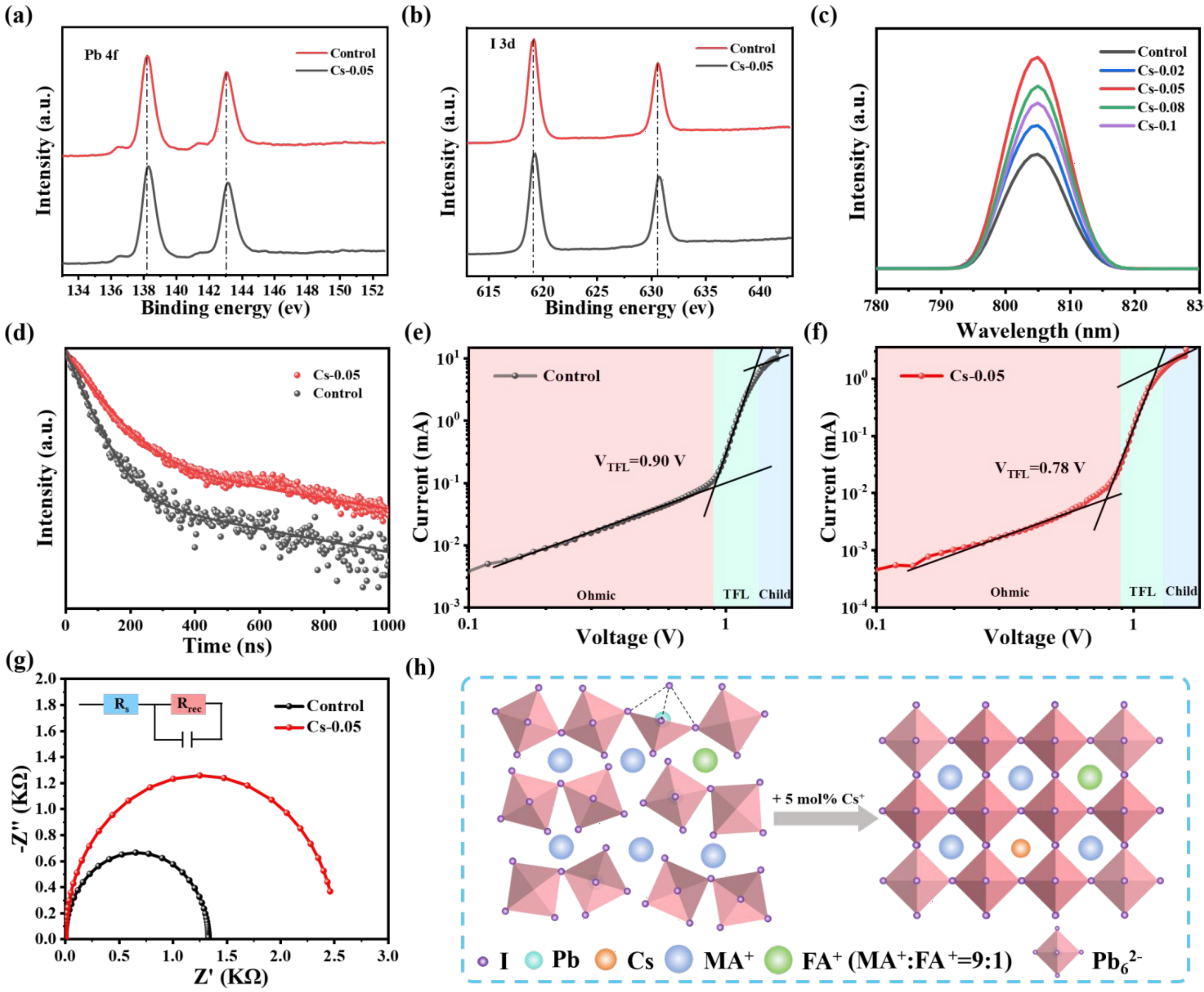

**Figure 3 a–b** XPS of the control and Cs–0.05 films: (a) Pb 4f; (b) I 3d. **c** PL spectra of the control and CsI–doped perovskite films; **d** TRPL decay spectra of the control and CsI–doped perovskite films. **e–f** SCLC test of (e) the control group and (f) the CsI doped device. **g** Nyquist plot at a bias voltage of 1 V. **h** Schematic illustration of the perovskite lattice with $Cs^+$ partially substituting A–site cations. The organic cations are drawn to reflect the MA–dominated composition ($MA^+$: $FA^+$=9:

View Article Online
DOI: 10.1039/D6NA00481D

1). The $Cs^+$ ion occupies an A–site position without preference for $MA^+$ or $FA^+$. This is a simplified 2D representation for illustrative purposes and is not drawn to scale.

To elucidate the impact of CsI doping on photovoltaic performance, devices with the structure ITO/$SnO_2$/perovskite/carbon electrode were fabricated using perovskite absorbers with varying CsI concentrations. Following systematic optimization of doping levels, the current density–voltage (J–V) characteristics of the champion PSC are presented in **Fig. 4a**, with corresponding photovoltaic parameters listed in **Table S4**. As shown in **Fig. 4d–g**, benefiting from CsI–induced synergistic enhancements in film morphology, optimized band alignment, and effective defect passivation, the optimized device achieves a PCE of 17.31% ($V_{OC}$ = 1.042 V, $J_{SC}$= 22.31 mA $cm^{-2}$, FF = 74.45%). This represents a substantial improvement over the control device (PCE = 13.25%, $V_{OC}$ = 1.002 V, $J_{SC}$ = 21.99 mA $cm^{-2}$, FF = 60.13%). Notably, supra–optimal CsI doping degrades device performance induced by lattice distortion–induced phase segregation. This triggers the nucleation of metastable non–perovskite phases, generating fine–grained microstructures with increased defect densities that impede carrier transport and extraction efficiency. Consequently, precise control of doping concentration is critical for maximizing PSC performance. To contextualize our results, the progress of representative carbon–based HTL–free PSCs was summarized in Table S5. Notably, the highest efficiencies in such devices have almost exclusively relied on additional organic passivators or interlayers. In contrast, our CsI–doped device achieves 17.31% PCE without any such additives, highlighting the effectiveness of this simple inorganic doping strategy. As shown in **Fig. 4h**, Our device achieved a remarkable PCE of 17.31%, which substantially outperforms not only single–cation $MAPbI_3$–based C–PSCs, but also surpasses the efficiency of many systems that rely on complex organic passivators. The superior performance of our device underscores a key advantage of our approach: the $Cs^+$ dopant itself acts as a multifunctional agent that simultaneously stabilizes the perovskite phase, induces

View Article Online
DOI: 10.1039/D6NA00481D

beneficial lattice contraction to suppress ion migration, and passivates defects, all without necessitating additional intricate organic additives. This streamlined, inorganic doping strategy provides a more direct and effective pathway to high–efficiency C–PSCs.

The external quantum efficiency (EQE) spectra of the devices are presented in **Fig. 4b**. The integrated $J_{SC}$ values for the control and Cs–0.05 devices are 19.89 and 20.81 mA cm$^{-2}$, respectively, consistent the J–V measurements. The dark J–V curves (**Fig. 4c**) reveal a significant reduction in leakage current for the CsI–doped devices, further confirming suppression of charge recombination in these systems [37]. To further probe recombination mechanisms, we analyzed the dependence of $V_{OC}$ on light intensity using Equation 5:

$$V_{OC}=\frac{nkT\,ln(I)}{q} \tag{5}$$,

where *k* is the Boltzmann constant, T is the absolute temperature, *q* is the elementary charge, *I* is the light Intensity, and the defect–induced non–radiative recombination factor (*n*) can be extracted, as shown in **Fig. S3a**. The target device exhibits a significantly smaller slope (1.92 KT/q) than the control device (2.21 KT/q), demonstrating suppressed non–radiative recombination [38]. The exponent factor (*α*) can be obtained based on the relation between $J_{SC}$ and light intensity (Equation 6):

$$J_{SC}\propto I^{\alpha} \tag{6}$$.

As shown in **Fig. S3b**, the *α* value increased from 0.9567 for the pristine device to 0.9846 for the CsI–treated device, indicating that CsI incorporation significantly inhibits the electron–hole recombination [39]. Operational stability was evaluated by tracking steady–state current density and power conversion efficiency (PCE) at the maximum power point (MPP). Under maximum power point (MPP) voltage tracking at AM 1.5G illumination for 150 seconds, the Cs–0.05 device achieved enhanced performance with a bias voltage of 0.84 V and a stabilized PCE of 16.89%, outperforming the control (0.73 V, 12.57%), showing faster response and better operational stability (**Fig. 4i**).

View Article Online
DOI: 10.1039/D6NA00481D

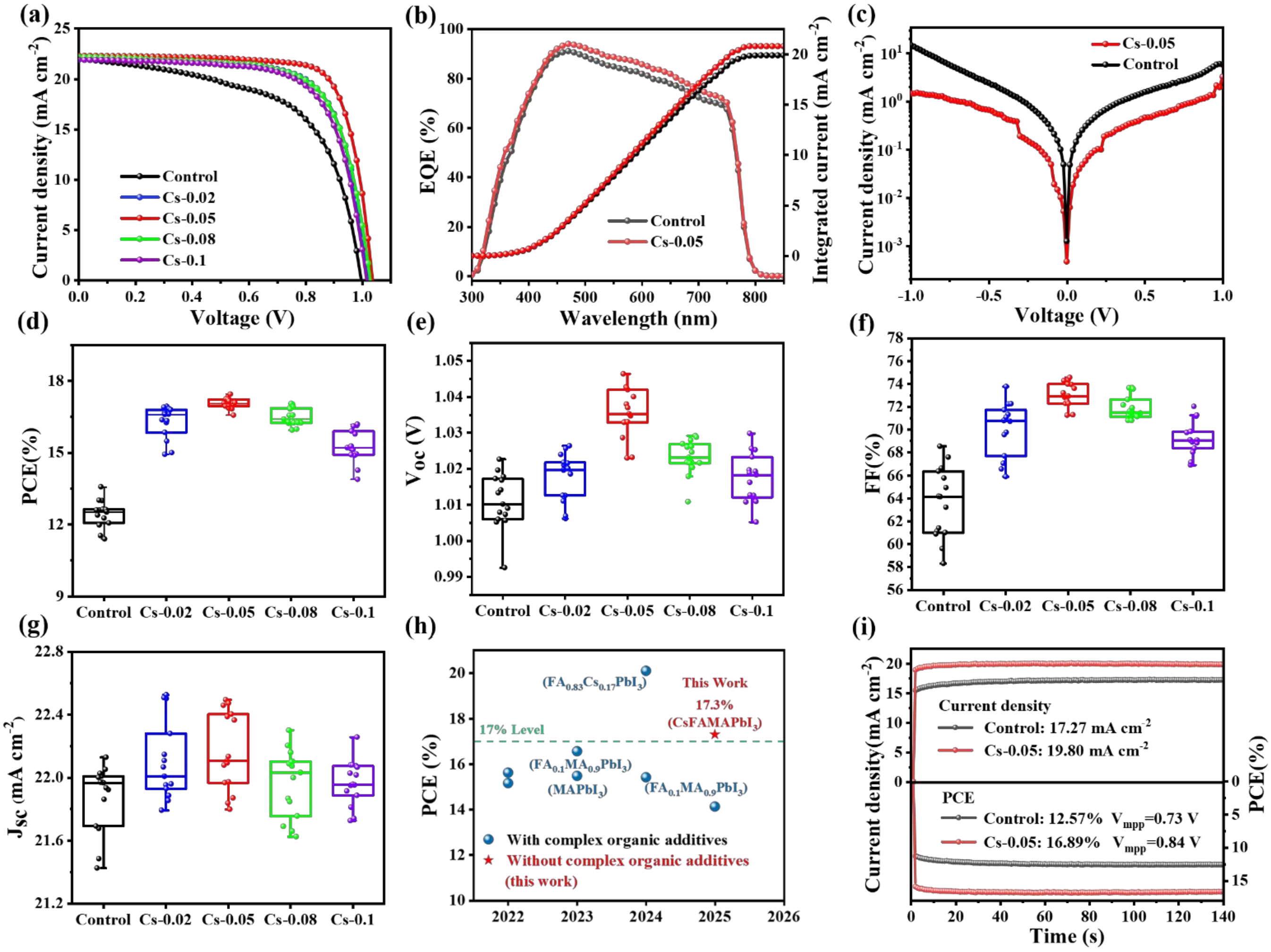

**Figure 4 a** J–V Characteristic Curves. **b** EQE curves of the respective devices. **c** Dark J–V curve of the control and CsI–doped devices. **d–g** Boxplot of Photovoltaic Parameters (15 devices): (d) PCE; (e) FF; (f) $V_{OC}$; (g) $J_{SC}$. **h** The PCE statistics of the representative previous studies and our champion device for typical HTL–free C–PSCs structure. **i** Steady–State Output Current and PCE at Maximum Power Point.

To assess the environmental stability, both control and CsI–doped films were aged under controlled conditions (25±5 °C, 55±5% RH). As shown in **Fig. 5a**, both films initially exhibited a similar black color, confirming the presence of a pure perovskite phase. After 5 days, the control film began to yellow at the edges, indicating the onset of hydration–induced degradation. By day 10, severe yellowing across the entire control film signaled extensive perovskite decomposition and probable crystal structure collapse. A complete

View Article Online
DOI: 10.1039/D6NA00481D

conversion to a pale yellow non–perovskite phase occurred by day 15. In stark contrast, the Cs–0.05 film maintained its original black color without visible degradation until day 10, showing only slight edge yellowing by day 15. These observations demonstrate that CsI doping significantly markedly enhances the intrinsic stability of the perovskite film by improving its crystallinity and resistance to moisture. The long–term operational stability of unencapsulated devices was further evaluated under ambient atmospheric conditions (20–25 ℃, 50–60% RH). As shown in **Fig. 5b**, the CsI–modified C–PSCs retained 73% of their initial PCE after 30 days, significantly outperforming the control devices, which degraded to 60% of their initial efficiency. This result underscores the critical role of CsI incorporation in ensuring the superior air stability of C–PSCs.

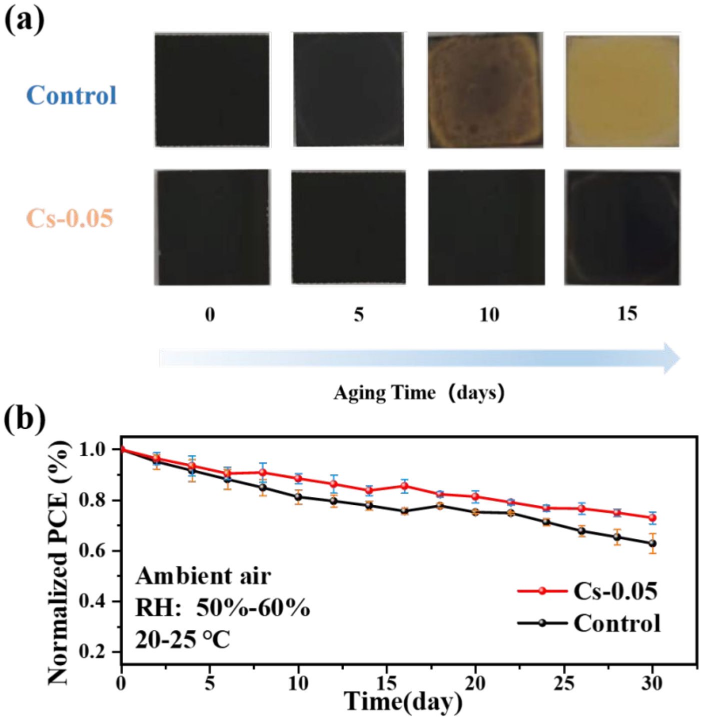

**Figure 5 a** Stability of the control and CsI–doped perovskite films in ambient air. **b** Stability of the control and CsI–doped perovskite solar cells in ambient air.

## 3. Conclusion

View Article Online
DOI: 10.1039/D6NA00481D

In summary, we have demonstrated that the incorporation of CsI into a binary MA–FA perovskite system serves as a simple yet highly effective strategy for synchronously enhancing the efficiency and stability of carbon–based, HTL–free PSCs. The $Cs^+$ ions play a multifunctional role: they induce lattice contraction, promote the growth of high–quality black phase crystals, suppress the formation of impurity phases and iodide vacancies, and reduce defect–mediated non–radiative recombination. These synergistic effects collectively contribute to a remarkable power conversion efficiency of 17.31%, enhanced by over 30% and significantly improved operational and environmental stability. This work underscores the great potential of inorganic cation engineering in developing high–performance, low–cost, and durable perovskite photovoltaics with simplified architectures.

## 4. Experimental Section

### Materials

Colloidal tin oxide nanoparticles ($SnO_2$, 15%) were procured from Alfa Aesar. High–purity chemical reagents, including N, N–dimethylformamide (DMF, 99.9%), dimethyl sulfoxide (DMSO, 99.9%), Chlorobenzene (CB, 99.9%), and isopropanol (IPA, 99.5%), were sourced from Sigma Aldrich. High–grade lead iodide ($PbI_2$, 99.99%) was obtained from TCI, while methylammonium iodide (MAI, 99.5%) and formamidinium iodide (FAI, 99.5%) were procured from Xi'an Yuri Solar Co., Ltd. Rubidium Chloride (CsI, 99.8%) was acquired from Sigma, and reliable carbon paste was sourced from Shanghai Materwin New Materials Co., Ltd.

### Device Fabrication

All devices were fabricated on etched ITO conductive glass substrates. The ITO glass substrates underwent a thorough cleaning regimen, commencing with ultrasonication in a sequential process involving anhydrous ethanol, detergent, ultrapure water, isopropanol, and anhydrous ethanol, each for 15 minutes.

View Article Online
DOI: 10.1039/D6NA00481D

Subsequently, they underwent an additional cleaning step, lasting 15 minutes, utilizing an ultraviolet ozone cleaner (UVO) before deployment. The $SnO_2$ colloidal solution was carefully diluted to a concentration of 5 wt% and applied via spin coating onto the ITO glass substrates. This process was carried out at 4000 rpm for 20 seconds, and the coated substrates were subsequently subjected to annealing at 150 ℃ for a duration of 30 minutes. The perovskite precursor solution was prepared by dissolving 691.5 mg of $PbI_2$, 214.6 mg of MAI, and 25.8 mg of FAI in a 1 mL mixed solution of DMSO and DMF, wherein the volume ratio of $V_{DMSO}$ to $V_{DMF}$ was maintained at 1:9. This solution was stirred continuously for 6 hours. Then, add the corresponding concentration of CsI to the solution and continue stirring for 2 hours. Subsequently, the precursor solution was spin–coated atop the $SnO_2$ layer at 4000 rpm for 30 seconds, with the timely addition of 150 μL of chlorobenzene (CB) as an anti–solvent within 6–7 seconds. This was followed by a meticulous annealing process at 120 ℃ for 10 minutes. Finally, a layer of carbon paste was expertly blade–coated directly onto the surface of the perovskite film and subsequently annealed at 100 ℃ for 10 minutes.

For each perovskite composition (control, Cs–0.02, Cs–0.05, and Cs–0.08), a batch of 20 devices was fabricated under identical conditions. After excluding short–circuited or visibly defective devices, the first 15 functional devices from each batch were used for statistical analysis of photovoltaic parameters. The sample size (n = 15) applies to all box plots presented in Fig. 4d–g.

## Characterization

The samples underwent X–ray diffraction (XRD) analysis utilizing a Cu Kα radiation X–ray diffractometer (Rigaku, Ultima IV). Surface morphology analysis was carried out using a Focused Ion Beam Scanning Electron Microscope (TESCAN, S9000X Xe Plasma FIB–SEM). Infrared (IR) spectroscopy was performed with a Fourier–transform infrared spectrometer (Bruker, INVENIO–S). Surface X–ray photoelectron spectroscopy spectra of the thin film samples were acquired utilizing an X–ray photoelectron

View Article Online
DOI: 10.1039/D6NA00481D

spectrometer (Thermo Science, K–Alpha). The UV–Visible absorption spectra of the thin film were measured using a UV–Visible spectrophotometer (Shimadzu, UV–1800). Use ultraviolet photoelectron spectroscopy (Thermo Science, Escalab Xi$^+$) to analyze the maximum value of the valence band in the film. Photoluminescence spectra and carrier lifetimes of the samples were obtained employing a time–resolved photoluminescence spectrometer (Edinburgh Instruments, FLS1000). Under dark conditions, the electrochemical impedance spectrum was measured using an electrochemical workstation(CH Instruments, CHI660E) at a bias voltage of 0.7 V applied to the device. Current–voltage (J–V) measurements were carried out with a Keithley 2461 source meter and a solar simulator (Enlitech, SS–X160R) under simulated AM 1.5G solar illumination (100 mW cm$^{-2}$).

## Competing interests

The authors declare that they have no known competing financial interests or personal relationships that could have appeared to influence the work reported in this paper.

## Data availability

The data supporting this article have been included as part of the supplementary information (SI). Supplementary information: local magnification of XRD (Fig. S1), a SEM image of the Cs–0.05 PVK film. b–d Distribution plots of (b) I, (c) Pb, (d) Cs (Fig. S2), a Light Intensity Dependence of VOC. b Light Intensity Dependence of JSC (Fig. S3), the statistical parameters of time–resolved photoluminescence (TRPL) spectra fitted by a bi–exponential function (Table S1), calculated parameters and trap density (Nt) of control and Cs–0.05 devices (Table S2), fitting parameters of C–PSCs from Nyquist plots (Table S3), photovoltaic parameters of the best–performing control and Cs–0.05 devices measured under both reverse and forward voltage scans (Table S3).

View Article Online
DOI: 10.1039/D6NA00481D

## Acknowledgements

The authors acknowledge support from the NSAF (no. U2230131), Priority Academic Program Development of Jiangsu Higher Education Institutions (PAPD), Jiangsu Collaborative Innovation Center for Advanced Inorganic Function Composites, Nanjing Tech University, Key Research and Development Program of Ningbo City (grant numbers no. 2023Z151), and the Major Science and Technology Special Project of Shanxi Province (Project Number: 202401060301013).

## Author contributions

**Zhe Tang**: Writing–original draft, Writing–review & editing, Data curation. **Jiawei Zhao**: Formal analysis, Data curation, Validation. **Heng Liu**: Funding acquisition. . **Baoting Huang**, **Fengling Hang** and **Niang Cheng**: Validation. **Zhen–guo Liu**: Funding acquisition, Supervision. **Peng–an Zong**: Writing–review & editing, Supervision.

View Article Online
DOI: 10.1039/D6NA00481D

# References

[1] M. Liu, M.B. Johnston, H.J. Snaith, Efficient planar heterojunction perovskite solar cells by vapour deposition, Nature 501 (2013) 395–398. https://doi.org/10.1038/nature12509.

[2] Best Research–Cell Efficiency Chart | Photovoltaic Research | NREL, (n.d.). https://www.nrel.gov/pv/cell–efficiency (accessed July 9, 2025).

[3] J. Liu, X. Chen, K. Chen, W. Tian, Y. Sheng, B. She, Y. Jiang, D. Zhang, Y. Liu, J. Qi, K. Chen, Y. Ma, Z. Qiu, C. Wang, Y. Yin, S. Zhao, J. Leng, S. Jin, W. Zhao, Y. Qin, Y. Su, X. Li, X. Li, Y. Zhou, Y. Zhou, F. Ling, A. Mei, H. Han, Electron injection and defect passivation for high–efficiency mesoporous perovskite solar cells, Science 383 (2024) 1198–1204. https://doi.org/10.1126/science.adk9089.

[4] H. Gao, K. Xiao, R. Lin, S. Zhao, W. Wang, S. Dayneko, C. Duan, C. Ji, H. Sun, A.D. Bui, C. Liu, J. Wen, W. Kong, H. Luo, X. Zheng, Z. Liu, H. Nguyen, J. Xie, L. Li, M.I. Saidaminov, H. Tan, Homogeneous crystallization and buried interface passivation for perovskite tandem solar modules, Science 383 (2024) 855–859. https://doi.org/10.1126/science.adj6088.

[5] Z. Huang, Y. Bai, X. Huang, J. Li, Y. Wu, Y. Chen, K. Li, X. Niu, N. Li, G. Liu, Y. Zhang, H. Zai, Q. Chen, T. Lei, L. Wang, H. Zhou, Anion–π interactions suppress phase impurities in $FAPbI_3$ solar cells, Nature 623 (2023) 531–537. https://doi.org/10.1038/s41586–023–06637–w.

[6] J. Liu, M. Zhang, X. Sun, L. Xiang, X. Yang, X. Hu, Z. Wang, T. Hou, J. Qin, Y. Huang, M. Abdi–Jalebi, X. Hao, Scalable Fabrication of Methylammonium–Free Wide–Bandgap Perovskite Solar Cells by Blade Coating in Ambient Air, Nano–Micro Lett. 17 (2025) 1–11. https://doi.org/10.1007/s40820–025–01838–6.

View Article Online
DOI: 10.1039/D6NA00481D

[7] K. Zhao, Q. Liu, L. Yao, C. Değer, J. Shen, X. Zhang, P. Shi, Y. Tian, Y. Luo, J. Xu, J. Zhou, D. Jin, S. Wang, W. Fan, S. Zhang, S. Chu, X. Wang, L. Tian, R. Liu, L. Zhang, I. Yavuz, H. Wang, D. Yang, R. Wang, J. Xue, peri–Fused polyaromatic molecular contacts for perovskite solar cells, Nature 632 (2024) 301–306. https://doi.org/10.1038/s41586–024–07712–6.

[8] H. Min, D.Y. Lee, J. Kim, G. Kim, K.S. Lee, J. Kim, M.J. Paik, Y.K. Kim, K.S. Kim, M.G. Kim, T.J. Shin, S. Il Seok, Perovskite solar cells with atomically coherent interlayers on $SnO_2$ electrodes, Nature 598 (2021) 444–450. https://doi.org/10.1038/s41586–021–03964–8.

[9] M.A. Uddin, P.J.S. Rana, Z. Ni, G. Yang, M. Li, M. Wang, H. Gu, H. Zhang, B.D. Dou, J. Huang, Iodide manipulation using zinc additives for efficient perovskite solar minimodules, Nat. Commun. 15 (2024). https://doi.org/10.1038/s41467–024–45649–6.

[10] Y. Deng, S. Xu, S. Chen, X. Xiao, J. Zhao, J. Huang, Defect compensation in formamidinium–caesium perovskites for highly efficient solar mini–modules with improved photostability, Nat. Energy. 6 (2021) 633–641. https://doi.org/10.1038/s41560–021–00831–8.

[11] Y. Wang, W. Li, Y. Yin, M. Wang, W. Cai, Y. Shi, J. Guo, W. Shang, C. Zhang, Q. Dong, H. Ma, J. Liu, W. Tian, S. Jin, J. Bian, Y. Shi, Defective MWCNT Enabled Dual Interface Coupling for Carbon-Based Perovskite Solar Cells with Efficiency Exceeding 22%, Adv. Funct. Materials. 32 (2022). https://doi.org/10.1002/adfm.202204831.

[12] N. Arora, M.I. Dar, S. Akin, R. Uchida, T. Baumeler, Y. Liu, S.M. Zakeeruddin, M. Grätzel, Low-Cost and Highly Efficient Carbon-Based Perovskite Solar Cells Exhibiting Excellent Long-Term Operational and UV Stability, Small 15 (2019). https://doi.org/10.1002/smll.201904746.

[13] H. Chen, S. Yang, Carbon-Based Perovskite Solar Cells without Hole Transport Materials: The Front Runner to the Market?, Advanced Materials 29 (2017). https://doi.org/10.1002/adma.201603994.

[14] X. Meng, J. Zhou, J. Hou, X. Tao, S.H. Cheung, S.K. So, S. Yang, Versatility of Carbon Enables All Carbon Based Perovskite Solar Cells to Achieve High Efficiency and High Stability, Advanced Materials 30 (2018). https://doi.org/10.1002/adma.201706975.

[15] Z. Wei, H. Chen, K. Yan, X. Zheng, S. Yang, Hysteresis–free multi–walled carbon nanotube–based perovskite solar cells with a high fill factor, J. Mater. Chem. A. 3 (2015) 24226–24231. https://doi.org/10.1039/c5ta07714a.

[16] N. Pellet, P. Gao, G. Gregori, T.–Y. Yang, M.K. Nazeeruddin, J. Maier, M. Grätzel, Mixed–Organic–Cation Perovskite Photovoltaics for Enhanced Solar–Light Harvesting, Angew. Chem. Int. Ed. 53 (2014) 3151–3157. https://doi.org/10.1002/anie.201309361.

[17] N.J. Jeon, J.H. Noh, W.S. Yang, Y.C. Kim, S. Ryu, J. Seo, S.I. Seok, Compositional engineering of perovskite materials for high–performance solar cells, Nature 517 (2015) 476–480. https://doi.org/10.1038/nature14133.

[18] Z. Li, M. Yang, J.–S. Park, S.–H. Wei, J.J. Berry, K. Zhu, Stabilizing Perovskite Structures by Tuning Tolerance Factor: Formation of Formamidinium and Cesium Lead Iodide Solid–State Alloys, Chem. Mater. 28 (2016) 284–292. https://doi.org/10.1021/acs.chemmater.5b04107.

[19] L. Wang, Md. Shahiduzzaman, E.Y. Muslih, M. Nakano, M. Karakawa, K. Takahashi, K. Tomita, J.M. Nunzi, T. Taima, Double–layer CsI intercalation into an $MAPbI_3$ framework for efficient and stable perovskite solar cells, Nano Energy 86 (2021) 106135. https://doi.org/10.1016/j.nanoen.2021.106135.

[20] K. Jiang, F. Wu, G. Zhang, P.C.Y. Chow, C. Ma, S. Li, K.S. Wong, L. Zhu, H. Yan, Inverted planar perovskite solar cells based on CsI–doped PEDOT:PSS with efficiency beyond 20% and small energy loss, J. Mater. Chem. A. 7 (2019) 21662–21667. https://doi.org/10.1039/c9ta08995k.

[21] S. Wang, H. Liu, H. Bala, B. Zong, L. Huang, Z. Guo, W. Fu, B. Zhang, G. Sun, J. Cao, Z. Zhang, A

View Article Online
DOI: 10.1039/D6NA00481D

highly stable hole–conductor–free Cs MA1–$PbI_3$ perovskite solar cell based on carbon counter electrode, Electrochimica Acta 335 (2020) 135686. https://doi.org/10.1016/j.electacta.2020.135686.

[22] X. Xu, K. Wang, F. Lu, Y. Cao, X. Zhou, Crystallization modulation and defect passivation in carbon–based perovskite solar cells using multifunctional group additive, Opt. Mater. 150 (2024) 115245. https://doi.org/10.1016/j.optmat.2024.115245.

[23] Q. Wang, J. Wan, S. Wu, X. Zhou, Improvement on the performance and stability of carbon–based perovskite solar cells by using APH additives, Colloids Surf. Physicochem. Eng. Asp. 727 (2025) 138305. https://doi.org/10.1016/j.colsurfa.2025.138305.

[24] Y.H. Park, I. Jeong, S. Bae, H.J. Son, P. Lee, J. Lee, C. Lee, M.J. Ko, Inorganic Rubidium Cation as an Enhancer for Photovoltaic Performance and Moisture Stability of $HC(NH_2)_2PbI_3$ Perovskite Solar Cells, Adv. Funct. Materials. 27 (2017). https://doi.org/10.1002/adfm.201605988.

[25] Y. Wu, X. Li, S. Fu, L. Wan, J. Fang, Efficient methylammonium lead trihalide perovskite solar cells with chloroformamidinium chloride (Cl–FACl) as an additive, J. Mater. Chem. A 7 (2019) 8078–8084. https://doi.org/10.1039/C9TA01319A.

[26] Y. Wang, J. Li, Y. Zhou, Z. Gao, W. Zhu, L. Liu, Interfacial defect mediated charge carrier trapping and recombination dynamics in $TiO_2$–based nanoheterojunctions, Journal of Alloys and Compounds 872 (2021) 159592. https://doi.org/10.1016/j.jallcom.2021.159592.

[27] T. Du, T.J. Macdonald, R.X. Yang, M. Li, Z. Jiang, L. Mohan, W. Xu, Z. Su, X. Gao, R. Whiteley, C.–T. Lin, G. Min, S.A. Haque, J.R. Durrant, K.A. Persson, M.A. McLachlan, J. Briscoe, Additive–Free, Low–Temperature Crystallization of Stable α–$FAPbI_3$ Perovskite, Advanced Materials 34 (2022) 2107850. https://doi.org/10.1002/adma.202107850.

[28] P. Holzhey, P. Yadav, S.–H. Turren–Cruz, A. Ummadisingu, M. Grätzel, A. Hagfeldt, M. Saliba, A

View Article Online
DOI: 10.1039/D6NA00481D

chain is as strong as its weakest link – Stability study of $MAPbI_3$ under light and temperature, Materials Today 29 (2019) 10–19. https://doi.org/10.1016/j.mattod.2018.10.017.

[29] H.D. Kim, H. Ohkita, H. Benten, S. Ito, Photovoltaic Performance of Perovskite Solar Cells with Different Grain Sizes, Advanced Materials 28 (2016) 917–922. https://doi.org/10.1002/adma.201504144.

[30] G. Zhou, J. Wu, Y. Zhao, Y. Li, J. Shi, Y. Li, H. Wu, D. Li, Y. Luo, Q. Meng, Application of Cesium on the Restriction of Precursor Crystallization for Highly Reproducible Perovskite Solar Cells Exceeding 20% Efficiency, ACS Appl. Mater. Interfaces 10 (2018) 9503–9513. https://doi.org/10.1021/acsami.8b01054.

[31] U. Kwon, M.M. Hasan, W. Yin, D. Kim, N.Y. Ha, S. Lee, T.K. Ahn, H.J. Park, Investigation into the Advantages of Pure Perovskite Film without $PbI_2$ for High Performance Solar Cell, Sci. Rep. 6 (2016). https://doi.org/10.1038/srep35994.

[32] A. Kausar, A. Sattar, C. Xu, S. Zhang, Z. Kang, Y. Zhang, Advent of alkali metal doping: a roadmap for the evolution of perovskite solar cells, Chem. Soc. Rev. 50 (2021) 2696–2736. https://doi.org/10.1039/d0cs01316a.

[33] S.–H. Lee, S. Jeong, S. Seo, H. Shin, C. Ma, N.–G. Park, Acid Dissociation Constant: A Criterion for Selecting Passivation Agents in Perovskite Solar Cells, ACS Energy Lett. 6 (2021) 1612–1621. https://doi.org/10.1021/acsenergylett.1c00452.

[34] X. Yuan, R. Li, Z. Xiong, P. Li, G.O. Odunmbaku, K. Sun, Y. Deng, S. Chen, Synergistic Crystallization Modulation and Defects passivation via Additive Engineering Stabilize Perovskite Films for Efficient Solar Cells, Adv. Funct. Materials 33 (2023). https://doi.org/10.1002/adfm.202215096.

View Article Online
DOI: 10.1039/D6NA00481D

[35] Z. Huang, L. Li, H. Rao, Z. Pan, X. Zhong, Air–Processed Carbon–Based $Cs_{0.5}FA_{0.5}PbI_3$–$Cs_4PbI_6$ Heterostructure Perovskite Solar Cells with Efficiency Over 16%, Solar RRL. 6 (2022) 2200145. https://doi.org/10.1002/solr.202200145.

[36] V.K. Sangwan, M. Zhu, S. Clark, K.A. Luck, T.J. Marks, M.G. Kanatzidis, M.C. Hersam, Low–Frequency Carrier Kinetics in Perovskite Solar Cells, ACS Appl. Mater. Interfaces 11 (2019) 14166–14174. https://doi.org/10.1021/acsami.9b03884.

[37] C. Li, Z. Song, D. Zhao, C. Xiao, B. Subedi, N. Shrestha, M.M. Junda, C. Wang, C.–S. Jiang, M. Al–Jassim, R.J. Ellingson, N.J. Podraza, K. Zhu, Y. Yan, Reducing Saturation–Current Density to Realize High–Efficiency Low–Bandgap Mixed Tin–Lead Halide Perovskite Solar Cells, Advanced Energy Materials 9 (2019) 1803135. https://doi.org/10.1002/aenm.201803135.

[38] Q. Chen, X. Yang, J. Zhang, J. Fu, Z. Jiang, B. Song, P. Xu, Y. Zhou, Defect passivation by a betaine–based zwitterionic molecule for high–performance p–i–n methylammonium–based perovskite solar cells, Solar Energy Materials and Solar Cells 264 (2024) 112615. https://doi.org/10.1016/j.solmat.2023.112615.

[39] Y. Miao, M. Zheng, H. Wang, C. Chen, X. Ding, C. Wu, B. Wang, M. Zhai, X. Yang, M. Cheng, In–situ secondary annealing treatment assisted effective surface passivation of shallow defects for efficient perovskite solar cells, Journal of Power Sources 492 (2021) 229621. https://doi.org/10.1016/j.jpowsour.2021.229621.

[40] The lattice reconstruction of Cs–introduced $FAPbI_{1.80}Br_{1.20}$ enables improved stability for perovskite solar cells, RSC Adv. 11 (2021) 3997–4005. https://doi.org/10.1039/d0ra09294k.

[41] A.A. Sutanto, V.I.E. Queloz, I. Garcia–Benito, K. Laasonen, B. Smit, M.K. Nazeeruddin, O.A. Syzgantseva, G. Grancini, Pushing the limit of Cs incorporation into $FAPbBr_3$ perovskite to enhance

View Article Online
DOI: 10.1039/D6NA00481D

solar cells performances, APL Mater. 7 (2019) 041110. https://doi.org/10.1063/1.5087246.

View Article Online
DOI: 10.1039/D6NA00481D

# Data Availability Statement

The data supporting this article have been included as part of the supplementary information (SI). Supplementary information: local magnification of XRD (Fig. S1), a SEM image of the Cs-0.05 PVK film. b-d Distribution plots of (b) I, (c) Pb, (d) Cs (Fig. S2), a Light Intensity Dependence of VOC. b Light Intensity Dependence of JSC (Fig. S3), the statistical parameters of time-resolved photoluminescence (TRPL) spectra fitted by a bi-exponential function (Table S1), calculated parameters and trap density (Nt) of control and Cs-0.05 devices (Table S2), fitting parameters of C-PSCs from Nyquist plots (Table S3), photovoltaic parameters of the best-performing control and Cs-0.05 devices measured under both reverse and forward voltage scans (Table S3).